crystals

MDPI

Article

Size Matters: New Zintl Phase Hydrides of *RE*Ga (*RE* = Y, La, Tm) and *RE*Si (*RE* = Y, Er, Tm) with Large and Small Cations

Anton Werwein [1], Thomas C. Hansen [2] and Holger Kohlmann [1,*]

[1] Leipzig University, Institute of Inorganic Chemistry, Johannisallee 29, 04103 Leipzig, Germany; anton.werwein@uni-leipzig.de

[2] Institut Laue-Langevin, 71 Avenue des Martyrs, CS 20156, CEDEX 9, 38042 Grenoble, France; hansen@ill.fr

* Correspondence: holger.kohlmann@uni-leipzig.de; Tel.: +49-341-9736201

Received: 18 October 2019; Accepted: 12 November 2019; Published: 16 November 2019

Abstract: Many Zintl phases exhibiting a CrB type structure form hydrides. Systematic studies of *AeTt*H_x (*Ae* = Ca, Sr, Ba; *Tt* = Si, Ge, Sn), *LnTt*H_x (*Ln* = La, Nd; *Tt* = Si, Ge, Sn), and *Ln*GaH_x (*Ln* = Nd, Gd) showed the vast structural diversity of these systems. Hydrogenation reactions on *RE*Ga (*RE* = Y, La, Tm) and *RESi* (*RE* = Y, Er, Tm) were performed in steel autoclaves under hydrogen pressure up to 5 MPa and temperatures up to 773 K. The products were analyzed by X-ray and neutron powder diffraction. *RE*Si (*RE* = Y, Er, Tm) form hydrides in the *C*-LaGeD type. $LaGaD_{1.66}$ is isostructural to $NdGaD_{1.66}$ and shows similar electronic features. Ga-D distances (1.987(13) Å and 2.396(9) Å) are considerably longer than in polyanionic hydrides and not indicative of covalent bonding. In $TmGaD_{0.93(2)}$ with a distorted CrB type structure deuterium atoms exclusively occupy tetrahedral voids. Theoretical calculations on density functional theory (DFT) level confirm experimental results and suggest metallic properties for the hydrides.

Keywords: Zintl phases; metal hydrides; interstitial hydrides; Zintl phase hydrides; lanthanides; powder diffraction; neutron diffraction; deuterides; thermal analysis; in situ diffraction

1. Introduction

Hydrogenation reactions of intermetallics yield a plethora of compounds with large variation in chemical bonding [1]. Zintl phase hydrides are particularly interesting since they combine different bonding modes. Moreover, oxidation of polyanions in Zintl phases by hydrogen is a subtle way to manipulate crystal and electronic structure and to tune physical properties. Zintl phases are polar intermetallic compounds consisting of an electropositive element *M* (alkali metal, alkaline earth metal, or rare earth metal) and an element *X* from group 13–16. The electrons of *M* are being formally transferred to *X*, which forms a polyanion with a connectivity equal to the isoelectronic element [2–5]. This simple counting scheme, known as the Zintl–Klemm rule, allows prediction of the connectivity of polyanions.

Zintl phases form various hydrides with two structural motifs highlighted [6]. The hydrogen atoms can be bound covalently to the polyanion (e.g., in $KSiH_3$), incorporated inside a polyhedral void with strong ionic interactions (e.g., LaSiH, Ca_3SnH_2) and even show both structural motifs at the same time (e.g., $BaSiH_2$) [7–10]. Despite the ionic or covalent bonding pattern, some of the hydrides keep their metallic character ($CaSiH_{4/3}$, $SrAl_2H_2$) [11,12]. Various examples showed that small deviations of the elemental combination result in the formation of different hydrides [12,13]. In this article, the family of Zintl phase hydrides will be extended by hydrides of *RE*Ga (*RE* = Y, La, Tm) and *RE*Si (*RE* = Y, Er, Tm). *RE*Ga compounds are known for all rare earth elements except Eu and Yb. They crystallize in the

CrB type structure (Figure 1), where gallium atoms are located in a trigonal prismatic void of RE_6 and are arranged as zig-zag chain [14]. The CrB type structure exhibits tetrahedral RE_4 voids, which are suitable for hydrogen incorporation (Figure 1). Rare earth gallides show some covalence in bonding between the *RE* and Ga ions and metallic conductivity. An ionic formula RE^{3+} Ga^{3-} with complete charge transfer is thus misleading [15]. Nevertheless, we will use the term Zintl phase, because main structural features can be easily explained with this concept.

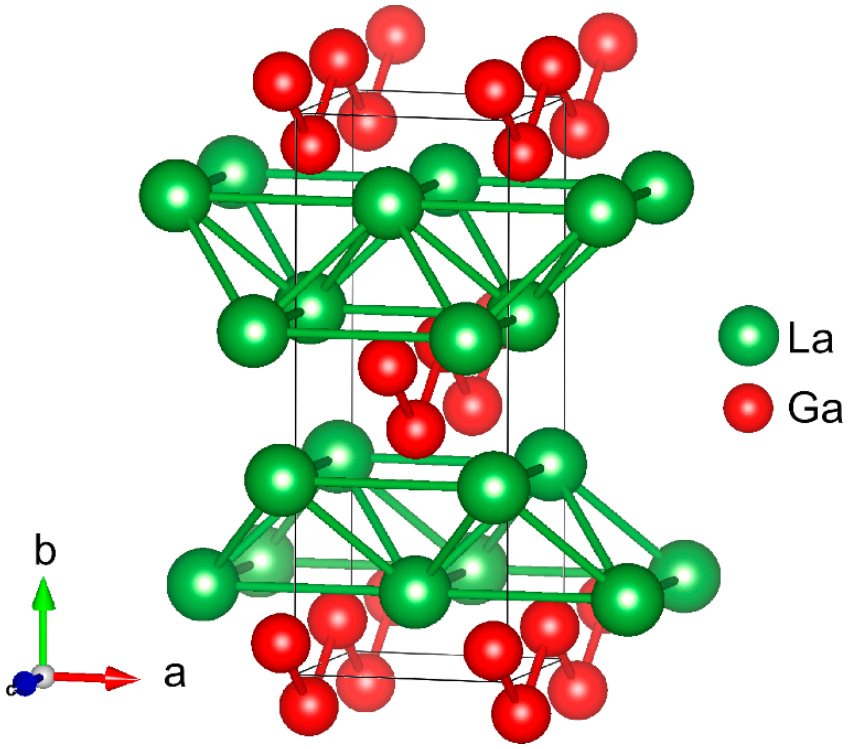

Figure 1. Crystal structure of LaGa; Ga zig-zag chains and tetrahedral voids are highlighted.

There are many examples for the hydrogenation of compounds with a CrB type structure, e.g., ZrNi or TbNi forming the metallic hydrides $ZrNiH_x$ (x = 1–3) and $TbNiH_{3.3}$ and the Zintl phases *AeTt* (*Ae* = Ca, Sr, Ba; *Tt* = Si, Ge, Sn), *LnTt* (*Ln* = La, Nd; *Tt* = Si, Ge, Sn), and *Ln*Ga (*Ln* = Nd, Gd) [8,10,16–21]. *AeTt* (*Ae* = Ca, Sr, Ba; *Tt* = Si, Ge, Sn) form polyanionic hydrides with different hydrogen content and polyanions with different degrees of condensation (chains, ribbons) determined by the atomic radius ratio r_{Ae}/r_{Tt}. A smaller r_{Ae}/r_{Tt} value favors the formation of covalent bonds between the chains to higher condensed ribbons. On the other hand, *LnTt* only incorporates hydrogen in tetrahedral voids, independent from the elemental combination (*Ln* = La, Nd; *Tt* = Si, Ge, Sn).

The first examples for hydrides of *Ln*Ga were NdGa and GdGa, forming $NdGaH_{1.66}$ and $GdGaH_{1.66}$, where Ln_4 tetrahedra are fully occupied by hydrogen atoms [20,21]. Furthermore, hydrogen atoms are found in two-thirds of the Ln_3Ga_2 trigonal-bipyramidal voids with a partial ordering, resulting in a threefold supercell. The hydrogen atom positions of $NdGaD_{1.66}$ were determined by neutron powder diffraction, while $GdGaD_{1.66}$ was only investigated by X-ray powder diffraction and DFT calculations.

Structural analyses revealed that hydrogen atoms are not located exactly in the center of the Nd_3Ga_2 void, resulting in two different Ga-D distances (2.01(6) Å and 2.12(5) Å), longer than usual covalent Ga-H distances like in $RbGaH_2$ (1.656(4) Å) or $SrGa_2H_2$ (1.686(6) Å) [12,22]. A similar coordination was also observed in $LaGa_2D_{0.71(2)}$ [23], where hydrogen atoms occupy La_3Ga_2 polyhedra. This structural motif was not seen in $AeTtH_x$ compounds, although the VEC of Tt^{2-} is identical to Ga^{3-} thus suggesting that cations play an important role for hydrogen bonding patterns.

Rare earth containing compounds offer the opportunity to vary the cation radius while maintaining the valence electron concentration thus enabling the investigation of the crystal chemistry as a function of the ion size.

2. Materials and Methods

2.1. Synthesis

Due to air sensitivity, all handlings were carried out in an argon-filled glove box. Intermetallic compounds with rare earth metals were synthesized from the elements in stoichiometric amounts (Y (smart-elements®, Vienna, Austria), 99.95%; La (smart-elements®, Vienna, Austria), ≥ 99.99%; Tm (smart-elements®, Vienna, Austria), 99.99%; surface cleaned mechanically and cut into small pieces; Ga (smart-elements®, Vienna, Austria), 99.99%) by fusing the starting materials in a water-cooled copper crucible of an arc furnace under 80 kPa argon atmosphere (dried over P_4O_{10}, molecular sieve, silica gel, and titanium sponge at 800 K). Ingots were turned over and remelted several times to ensure homogeneity. Gallium excess of up to 50% was used in order to avoid a secondary phase, which could not be identified as one of the known lanthanum gallium compounds. The hydrides (deuterides) were prepared from well-ground samples of the intermetallic precursors in crucibles made from hydrogen-resistant L718-V alloy (Böhler, Kapfenberg, Austria) and reacted with hydrogen (deuterium) gas (hydrogen (Air Liquide, Paris, France), 99.9%; deuterium (Air Liquide, Paris, France), 99.8%), at hydrogen gas pressures of 1.0 MPa ($YGaD_x$), 2.0 MPa ($LaGaD_x$), and 5.0 MPa (*RE*SiHx). The temperature was increased with a rate of 100 K/h to 573 K for the gallides and 773 K for the silicides, held for 48 h, and cooled by switching off the furnace.

2.2. Thermal Analysis

Hydrogenation experiments were carried out in a differential scanning calorimeter (DSC) Q1000 (TA Instruments, New Castle, Delaware, USA) equipped with a gas pressure cell. Powdered samples weighing 10–30 mg were loaded into aluminum pans, which were subsequently crimped. The experiments were performed under isochoric conditions with a heating rate of 10 K/min under 1.0 MPa hydrogen at 298 K at the final temperature of 703 K.

2.3. X-ray Powder Diffraction (XRPD)

X-ray powder diffraction data on flat transmission samples were collected on a G670 camera (Huber, Rimsting, Germany) with image-plate detection system and capillary samples were measured on a STADI P diffractometer (STOE, Darmstadt, Germany), both with Cu-Kα1 radiation. Flat transmission samples were prepared by grinding and mixing the moisture sensitive powders with Apiezon grease under an argon atmosphere and placing the sample between two sheets of Kapton foil.

2.4. Neutron Powder Diffraction (NPD)

Neutron powder diffraction was carried out at the Institut Laue-Langevin in Grenoble, France, at the high flux diffractometer D20 in high-resolution mode. Powdered samples (3 g) were held in gas-tight vanadium containers with a 6-mm inner diameter, and the measurement time was 30 min. The wavelengths were calibrated using silicon (NIST640b) as an external standard (λ = 1.86843(2) Å). Deuterides instead of hydrides were used in order to avoid the high incoherent scattering of ^{1}H.

2.5. In Situ Neutron Powder Diffraction

In situ neutron powder diffraction (NPD) was done at the high-intensity two-axis diffractometer D20 [24] at the Institute Laue-Langevin (ILL), Grenoble, France. The wavelength λ = 1.86563(5) Å was calibrated using an external silicon NIST640b standard sample in a 5 mm vanadium container. Time resolved neutron diffraction were collected under deuterium pressure and heating. These in situ experiments were carried out in (leuco-)sapphire single-crystal cells with 6 mm inner diameter

connected to a gas supply system. Details are given elsewhere [25]. The sample cell was filled with TmGa within a glove box and attached to the gas supply system, which was subsequently flushed with D_2 gas (deuterium (Air Liquide, Paris, France), 99.8% isotope purity). The reaction chamber was opened to the D_2 line at 0.1 MPa D_2 and ambient temperature which already allowed gas diffusion into the cell. Heating was realized using two laser beams. The sample was heated up to 500 K under 1 MPa deuterium pressure, cooled down to room temperature, heated under dynamic vacuum up to 500 K and cooled down to room temperature again.

Data sets were obtained with 2 min time resolution. They are presented with an additional internal raw label (NUMOR), referring to proposal 5-24-616 [26]. For the Rietveld refinement of $TmGaD_{0.93(2)}$ the NUMORs 132440 to 132447 were merged.

2.6. Rietveld Refinement

Rietveld refinements [27,28] were performed using TOPAS [29] and FULLPROF [30,31]. Deuterium atoms were located by difference Fourier analysis. Crystal structures were visualized with VESTA [32,33]. Further details of the crystal structure investigations may be obtained from FIZ Karlsruhe, 76344 Eggenstein-Leopoldshafen, Germany (fax: (+49)7247-808-666; e-mail: crysdata@fiz-karlsruhe.de), on quoting the deposition number CSD-1918940 ($LaGaD_{1.63}$), 1918944 ($YSiH_x$), 1952988 ($TmGaD_{0.93}$) 1918941 ($YGaH_x$), 1918943 ($ErSiH_x$), and 1918945 ($TmSiH_x$).

2.7. Density Functional Theory (DFT) Calculations

DFT calculations were performed with the Abinit software package [34–38] using generalized gradient approximation (GGA) and the Perdew-Burke-Ernzerhof (PBE) functional [39]. Projector augmented wave (PAW) [40] atomic data were taken from the JTH PAW atomic dataset table [41,42]. The convergence of calculations was tested regarding kinetic energy cutoff, k-point grid, and smearing of metallic occupation levels with an accuracy of 0.1 mHartree. The kinetic energy cutoff (ecut) was set to 35 Hartree (pawecutdg = 70 Hartree). The compounds were treated metallic with 1 mHartree Gaussian smearing (occopt = 7, tsmear = 0.001). The smearing contribution of the total energy was lower than 0.1 mHartree. The hydrogen-containing structures were treated similarly. The used Monkhorst-Pack grids [43] are shown in the supplementary material. Lattice parameters reproduce experimental data with less than 1% deviation. The integration of the DOS was performed using the tetrahedron method.

3. Results

3.1. Hydrogenation Reactions

The hydrogenation of *RE*Si (RE = Y, Er, Tm) yielded compounds with CrB type structure with a reduced *a* and an expanded *b* lattice parameter, while *c* shows almost no change (Supplementary Materials Figures S1–S3, Tables S1–S3). These results are similar to those in *LnTt*H_x [8] and comparable to LaGa. Thermal analysis (DSC) of TmGa under hydrogen gas pressure shows an exothermic signal at 430 K (Figure S4). The hydrogenation products of YGa and TmGa show at least two hydride phases (Figure 2).

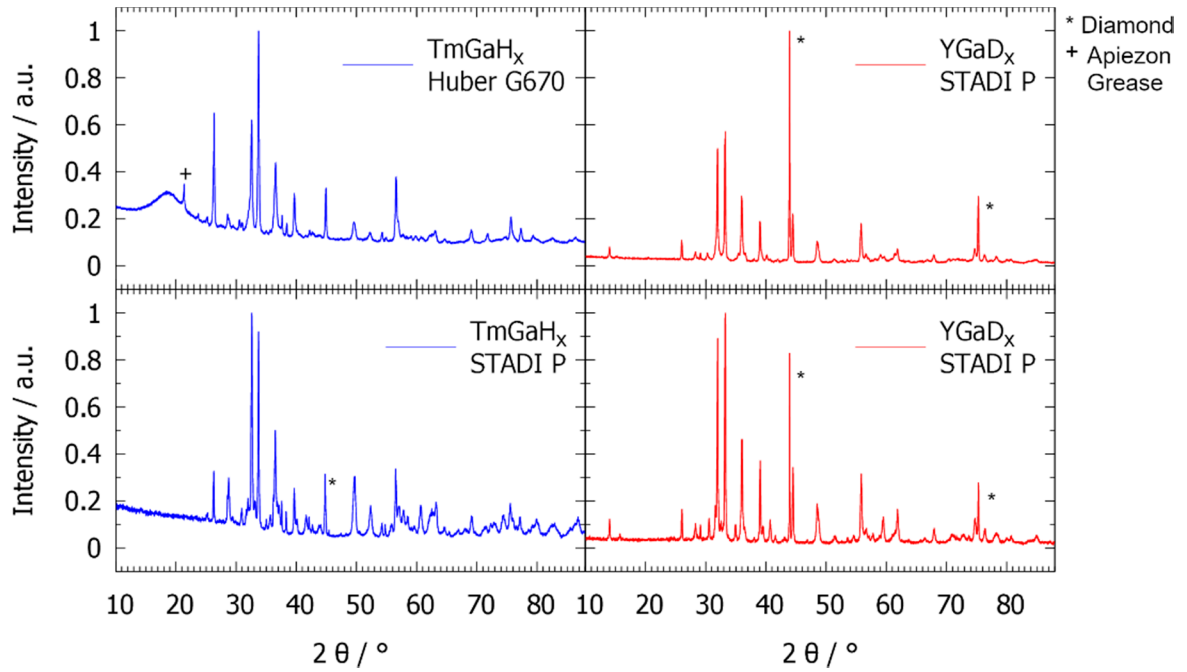

Figure 2. First row: X-ray powder diffraction patterns of $TmGaH_x$ and $YGaD_x$ after synthesis in the autoclave; **second row**: X-ray powder diffraction patterns of $TmGaH_x$ and $YGaD_x$ after storage under argon (glove box) for one week. All patterns were collected with Cu-Kα1 radiation.

XRPD patterns from hydrogenation products of the DSC experiments exhibit superstructure reflections which can be indexed to a 3*a* supercell with respect to the intermetallic parent material, while products gained by autoclave synthesis show somewhat broader and asymmetric reflections. After storage under argon (glove box) for one week the XRPD patterns change and are comparable to those of hydrogenation products from the DSC experiments (Figure 2). This finding points at the existence of hydrogen-rich and hydrogen-poor phases of $YGaH_x$ and $TmGaH_x$ and a sluggish hydrogen loss at room temperature.

3.2. Crystal Structures of the Hydrides

The neutron powder diffraction data of $LaGaD_{1.63(1)}$ exhibit reflections which cannot be indexed with a simple CrB type model, indicating a further superstructure (Figure 3). Using a 3*a* supercell and $LaGa_2D_x$ as side phase allows matching all reflections and a Rietveld refinement leads to a good correspondence of measured and calculated diffraction pattern. $LaGaD_{1.63(1)}$ is isotypic to $NdGaD_{1.66}$, whose crystal structure can be described as a deuterium filled CrB type superstructure (Figure 3, Table 1). Deuterium atoms in DLa_4 tetrahedra exhibit La-D distances ranging from 2.386(12) Å to 2.613(5) Å, comparable to other ionic lanthanum containing hydrides [44]. DLa_4 tetrahedra layers are slightly corrugated. Deuterium atoms inside La_3Ga_2 voids are off-center with two different Ga-D distances (1.987(11) Å and 2.396(8) Å), which show an even larger difference than those in $NdGaD_{1.66}$ (2.01(6) Å and 2.12(5) Å). The D-La distances are 2.347(4) Å and 2.469(9) Å. La_3Ga_2 voids in 8*c* Wyckoff position are nearly completely occupied, while the corresponding 4*a* void remains empty (Table 1). Two bipyramids are connected via a common corner with long Ga-D distances (Figure 4).

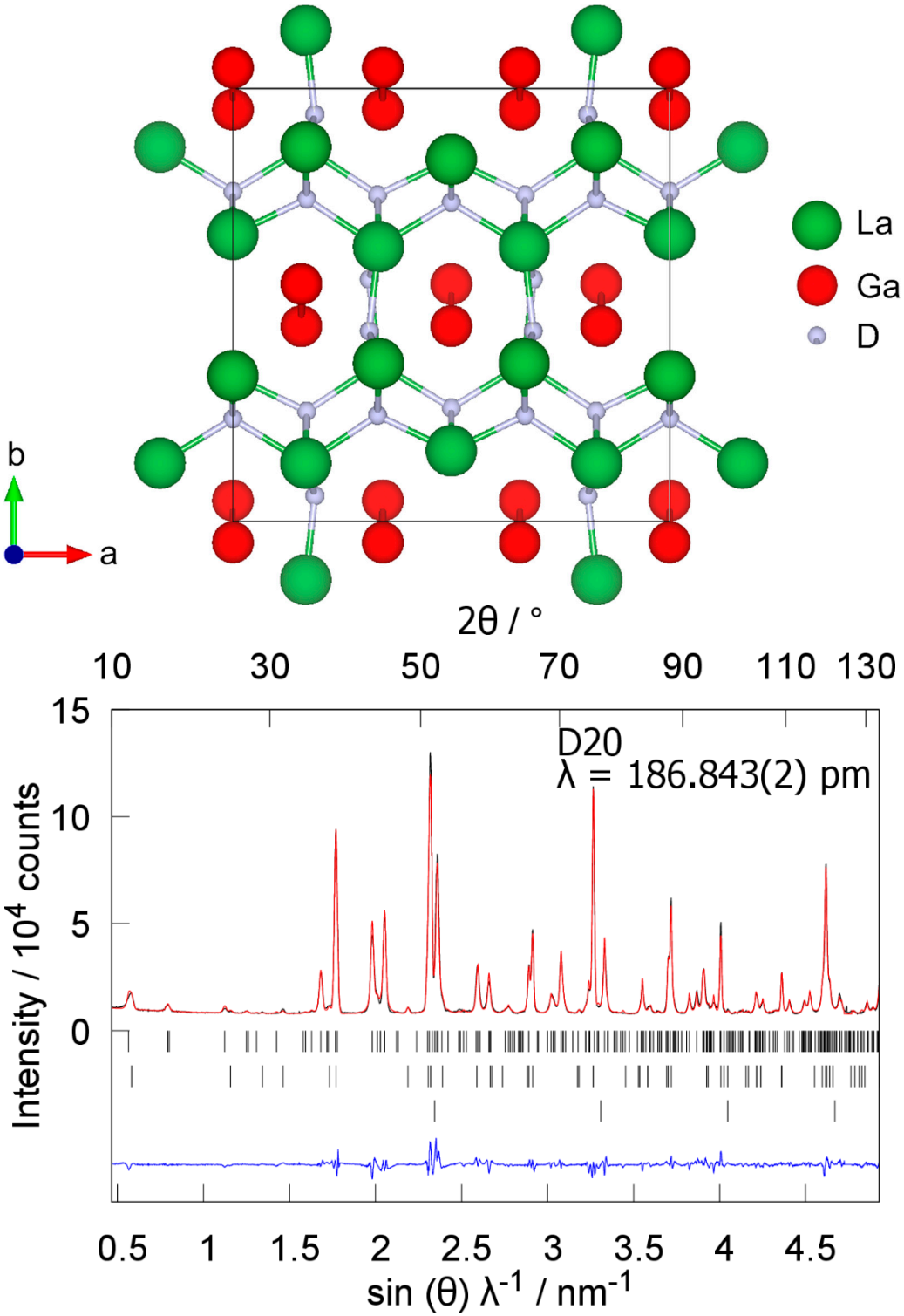

Figure 3. Top: crystal structure of $LaGaD_{1.63(1)}$; **bottom**: Rietveld refinement of the crystal structure of $LaGaD_{1.63(1)}$ using neutron powder diffraction data, Bragg marker from top to bottom: $LaGaD_{1.63(1)}$ (57.7(7)%), $LaGa_2D_{0.71}$ (45.3(5)%), V (sample container), R_p = 4.55%, R_{wp} = 6.05 %, GooF = 7.16.

Table 1. Crystal structure of $LaGaD_{1.63(1)}$ derived from neutron diffraction data, *Cmcm*, *a* = 12.7414(6) Å, *b* = 12.6178(6) Å, *c* = 4.2589(2) Å.

Atom	Site	*x*	*y*	*z*	B_{iso}/Å^2	*s.o.f*
La1	4*c*	0	0.3366(7)	1/4	1.07(8)	1
La2	8*g*	0.3333(7)	0.3651(4)	1/4	B_{iso}(La1)	1
Ga1	4*c*	0	0.0484(8)	1/4	1.83(8)	1
Ga2	8*g*	0.3456(7)	0.0487(7)	1/4	B_{iso}(Ga1)	1
D1	4*c*	0	0.7627(9)	1/4	2.32(9)	1
D2	8*g*	0.1689(9)	0.2549(7)	1/4	B_{iso}(D1)	1
D3	8*g*	0.1877(7)	0.0596(7)	1/4	3.1(2)	0.946(14)

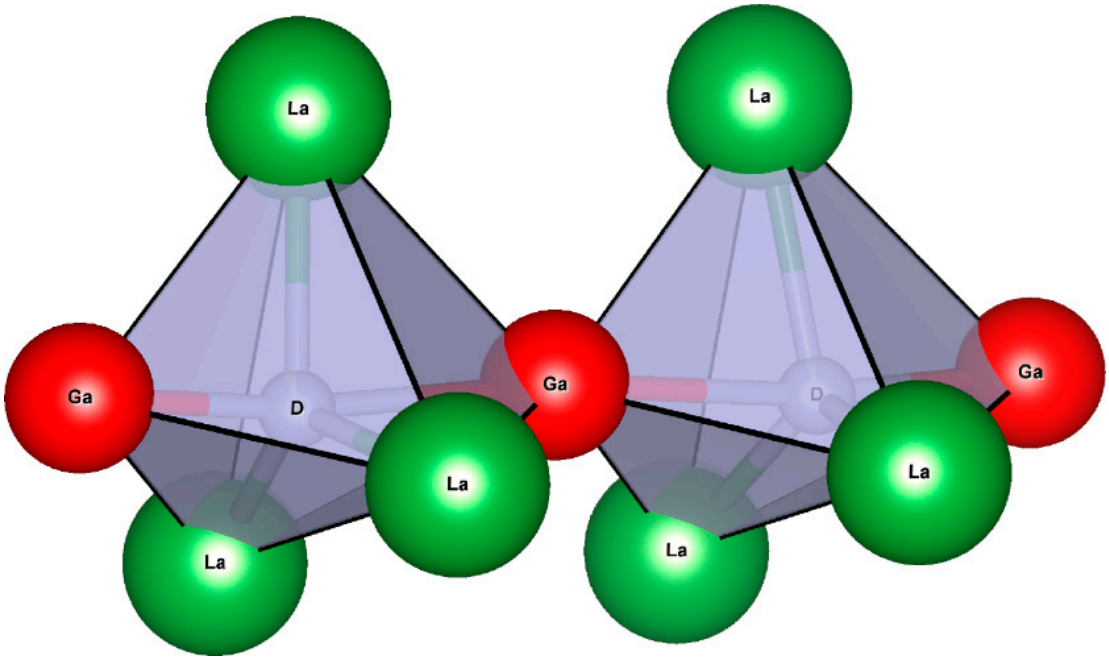

Figure 4. Two DLa_3Ga_2 coordination polyhedra in $LaGaD_{1.63(1)}$ connected via a common corner.

The structure of the non-hydrogen atoms of $TmGaH_x$ was solved by X-ray powder diffraction. Hydrogen atoms were localized by neutron powder diffraction on deuterides, derived by the in situ experiment (see Section 3.1).

$TmGaD_{0.93(2)}$ also exhibits a 3*a* superstructure of the CrB type. In contrast to $LaGaD_{1.63(1)}$, only tetrahedral voids are filled (Figure 5, Table 2). The DTm_4 containing layers are corrugated. D-Tm distances of 2.259(4) Å and 2.271(6) Å are in accordance with other Tm containing ionic hydrides [45]. The distances between gallium chains alternate (2.950(7) Å, 4.017(4) Å), caused by the deformation of the tetrahedral layer. XRPD data suggest $YGaH_x$ to be isostructural to $TmGaD_{0.93(2)}$. Structure distortions due to lanthanide contraction are also known for other systems [46].

Table 2. Crystal structure of $TmGaD_{0.93(2)}$, *Cmcm*, *a* = 10.9690(5) Å, *b* = 12.3722 (6) Å, *c* = 4.0373 (1) Å.

Atom	Site	*x*	*y*	*z*	B_{iso}/Å^2	*s.o.f*
Tm1	4*c*	0	0.3115(5)	1/4	0.91(6)	1
Tm2	8*g*	0.3190(4)	0.3585(4)	1/4	B_{iso}(Tm1)	1
Ga1	4*c*	0	0.0592(5)	1/4	1.32(7)	1
Ga2	8*g*	0.3658(4)	0.0575(4)	1/4	B_{iso}(Ga1)	1
D1	4*c*	0	0.7705(5)	1/4	1.25(9)	0.93(1)
D2	8*g*	0.1751(5)	0.2367(4)	1/4	B_{iso}(D1)	0.93(1)

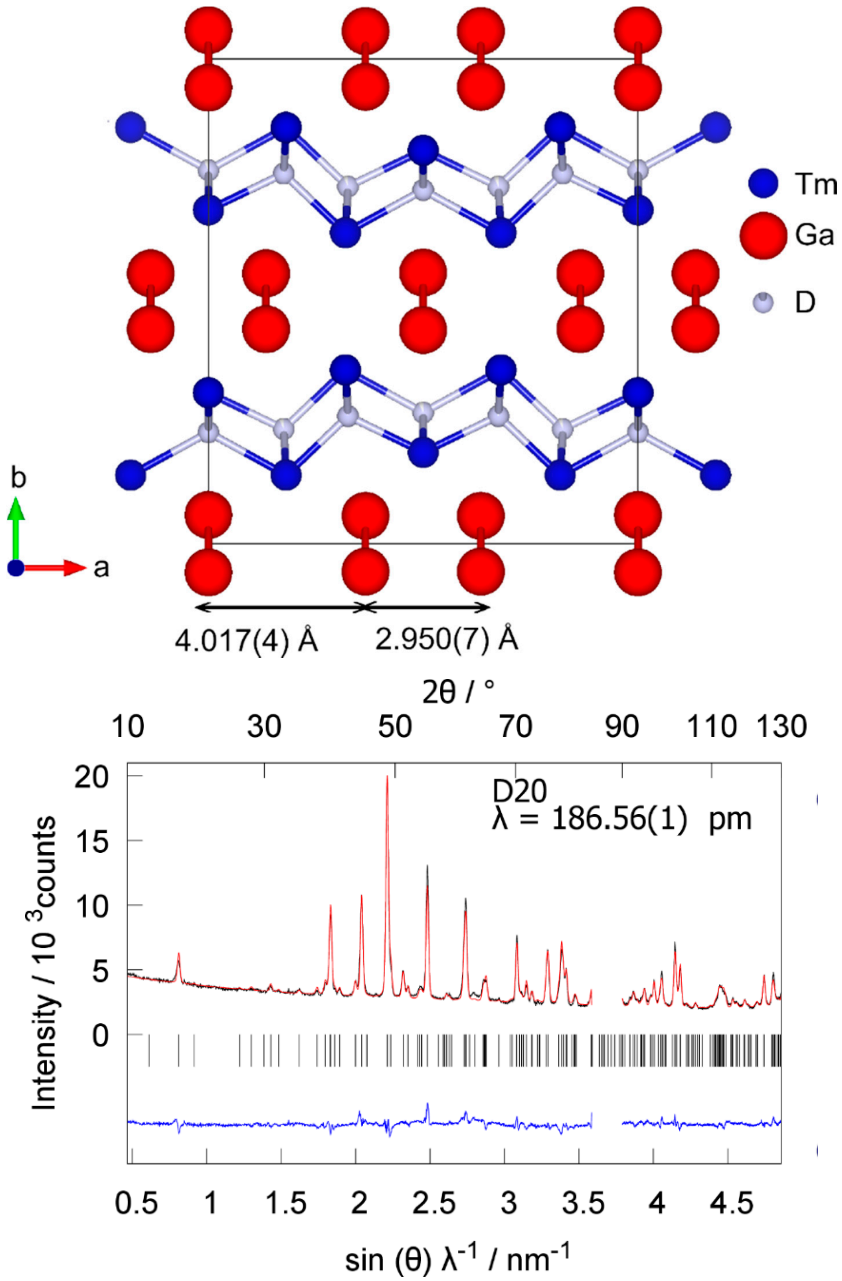

Figure 5. Top: crystal structure of $TmGaD_{0.93(2)}$; **bottom**: Rietveld refinement of the crystal structure of $TmGaD_{0.93(2)}$ derived from in situ neutron diffraction, $84° \leq 2\Theta \leq 90°$ excluded because of a strong reflection of the sample container, R_p = 4.08%, R_{wp} = 5.27%, GooF = 3.08.

3.3. Density Functional Theory (DFT) Calculations

The crystal structure of LaGa, LaGaH (a hypothetical intermediate product), and $LaGaH_{1.66}$ as well as YGa and YGaH in two different modifications (one hypothetical simple filled CrB type structure and one distorted) were optimized by DFT methods. The experimental crystal structures were used as a starting model and the total energies were minimized by structure relaxation. Lattice parameters are in good accordance to the experimental values (Table 3). The lattice parameter *a* decreases from 4.57 Å (LaGa) over 4.35 Å (LaGaH) to 4.27 Å ($LaGaH_{1.66}$), while *b* increases and *c* stays nearly unchanged. The Ga–Ga distance decreases during the oxidation from LaGa (2.63 Å) to LaGaH (2.54 Å) and increases again by further oxidation to $LaGaH_{1.66}$ (2.59 Å). A hydrogen atom in the center of the La_3Ga_2 void of the structure model for $LaGaH_{1.66}$ moved away to an off-center position during the optimization.

The Ga–H distances (1.88 Å and 2.55 Å) fit qualitatively the experimental results. DFT calculations on $NdGaH_{1.66}$ lead to the same results, with a similar discrepancy between theory and experiment [20]. All three compounds show density of states at the Fermi level and can be considered metallic. The main contribution at the Fermi Level are La-d and Ga-p states, which are shifted to higher energy by the oxidation with hydrogen. The Ga–Ga distance first shrinks (LaGaH), mainly by the depopulation of π^* states, and expands by further hydrogen incorporation ($LaGaH_{1.66}$). The lattice parameter of YGa and YGaH (distorted modification) could also be reproduced. The lattice parameter of hypothetical YGaH (*C*-LaGeH type) differ tremendously from the distorted variant, even though the lattice parameter changes have the same quality (*a* shrinks, *b* expands). Again, the Ga–Ga bond lengths become smaller (2.64 Å → 2.49 Å and 2.52 Å), upon the depopulation of π^* states. The alternating Ga–Ga interchain distances could also be reproduced by the theoretical calculation (2.88 Å and 4.13 Å).

Table 3. Lattice parameter of the structure optimized compounds (superstructures are normalized to one CrB unit cell).

Compound	*a*/Å	*b*/Å	*c*/Å	$d_{Ga\text{-}Ga}$/Å	*V*/Å^3
LaGa	4.566	11.606	4.235	2.634	224.42
LaGaH	4.349	12.461	4.270	2.536	231.43
$LaGaH_{1.66}$	12.819/4.27	12.603	4.276	2.591	690.88/230.12
YGa	4.339	10.971	4.064	2.640	193.44
YGaH (*C*-LaGeH type)	4.064	11.514	4.076	2.471	190.75
YGaH (α-TmGaH type)	11.146/3.71	12.707	4.093	2.493 2.516	579.76/193.25

The chemical bonding of hydrogen atoms can be partially deduced from the DOS and pDOS (Figures 6 and 7). The tetrahedrally coordinated hydrogen atoms of $LaGaD_{1.66}$ show a small dispersion in the pDOS for H-s states and La-d states in the same energy range as well for LaGaH as well as for $LaGaH_{1.66}$ and can be considered ionic. This is supported by the D–La bond length (2.44 Å–2.49 Å) which is in agreement with further ionic La containing hydride in tetrahedral coordination. The second hydrogen atom in $LaGaH_{1.66}$ cannot be called ionic anymore. Even though the La–D distance is similar (2.47 Å–2.51 Å), the pDOS shows a broad dispersion. The DOS in the range between −4 eV and −3 eV show an interaction with La-d states. This is also consistent with charge distribution of the hydrogen atoms of $NdGaH_{1.66}$, where hydrogen atoms inside a Nd_4 tetrahedra have a higher negative Bader charge (−0.65) than the hydrogen atoms in a La_3Ga_2 coordination (−0.51) indicating different bonding types. The electronic structure of YGa resembles that of LaGa (Figure 7). The electrons at the Fermi level are mainly contributed from Y-d and Ga-p states and represent a metallic conductor. The hydrogenation shifts the Fermi level to lower energies by the depopulation of La-d and Ga-p states. The H-s states show a small dispersion in analogy to LaGaH and overlap with Y-d states, suggesting ionic bonding. The pDOS of the Ga atoms are showing differences regarding the dispersion of the states indicating different bonding and coordination.

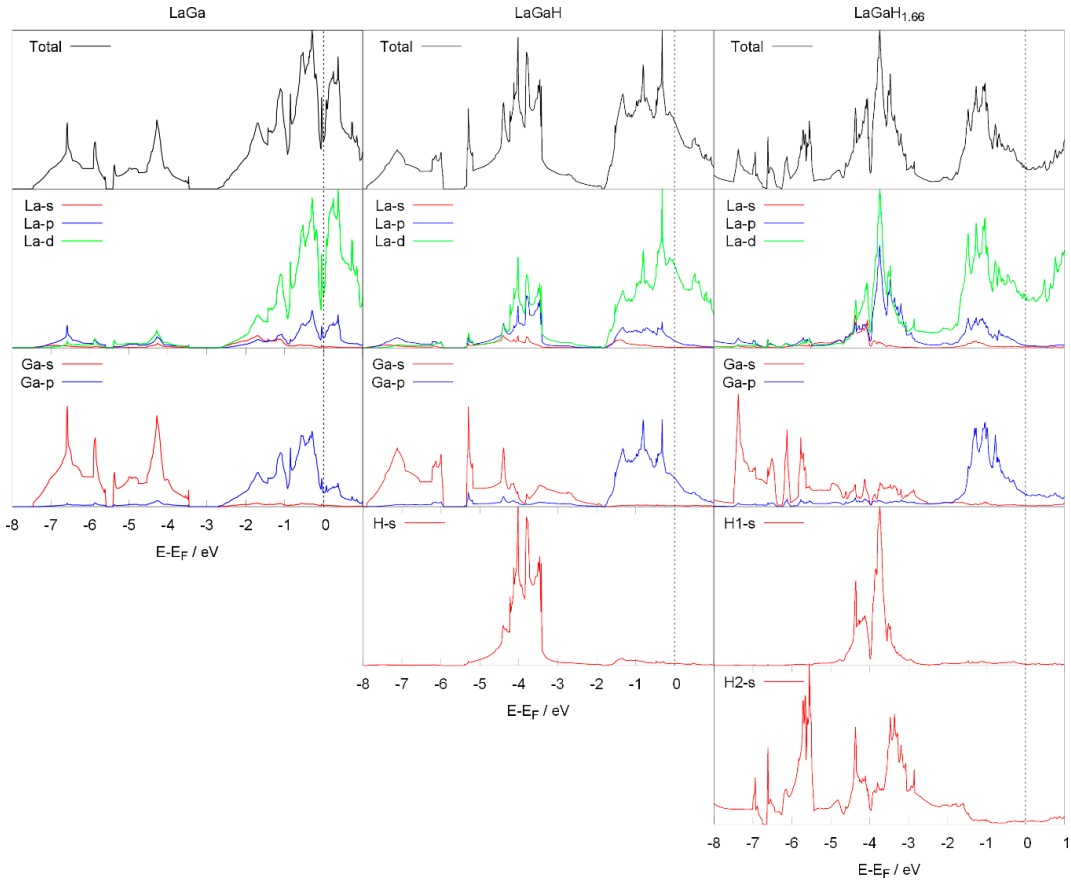

Figure 6. Calculated density of states of LaGa (**left**), LaGaH (**middle**), and $LaGaH_{1.66}$ (**right**) with black dotted lines indicating the Fermi level.

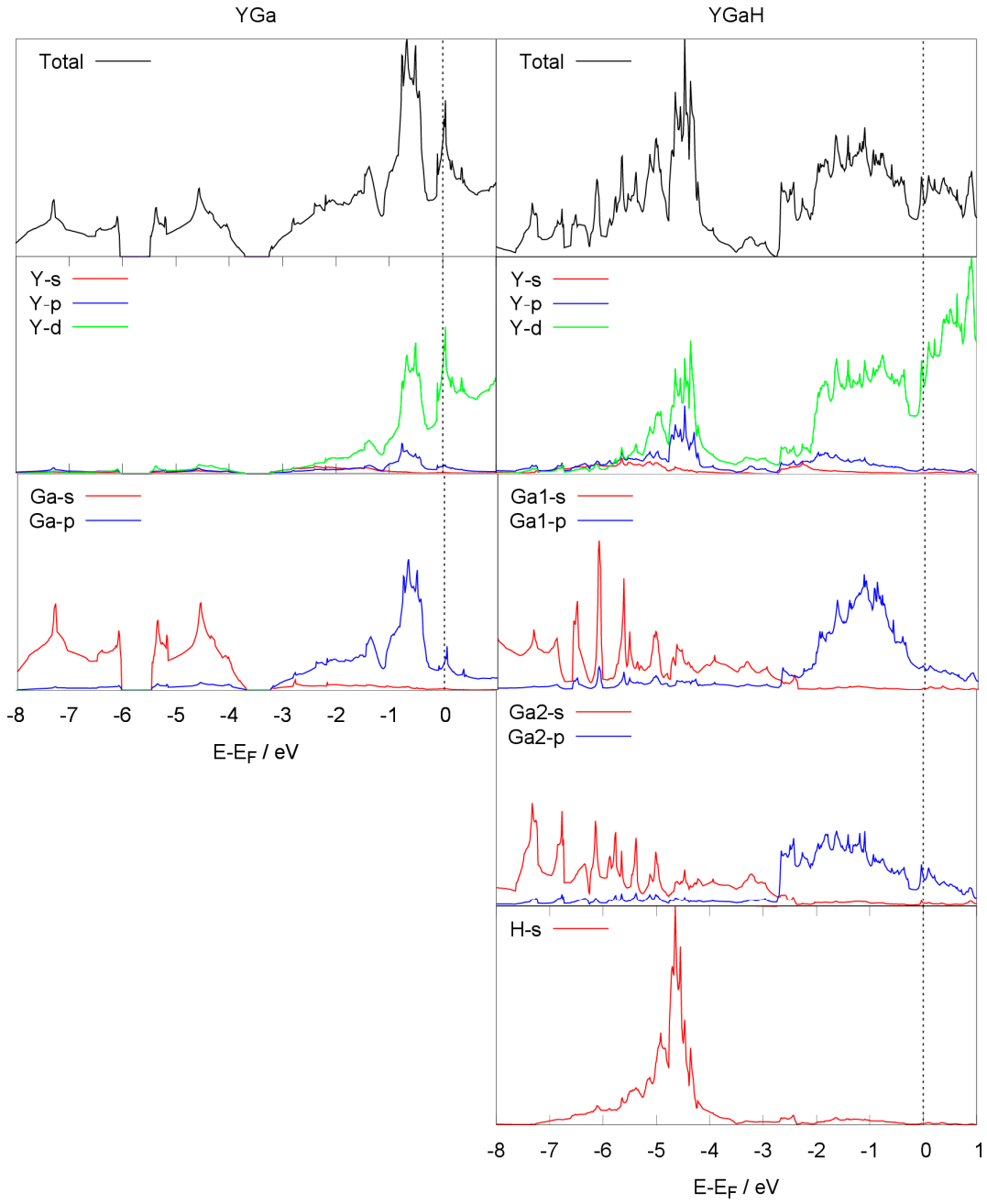

Figure 7. Calculated density of states of YGa (**left**) and YGaH (**right**) with black dotted lines indicating the Fermi level.

4. Discussion

The different structural features of CrB type related Zintl-phase hydrides are well represented by lattice parameter ratios (Figure 8, Table 4). All hydrogenation reactions result in similar qualitative changes. One driving force of the hydrogenation is the strong ionic interaction of hydride ions inside tetrahedral voids, which causes an expansion in *b* and contraction in *a*. The *b*/*a* value is thus suitable for categorizing different Zintl phase hydrides. However, *a* and *b* are not completely independent from each other.

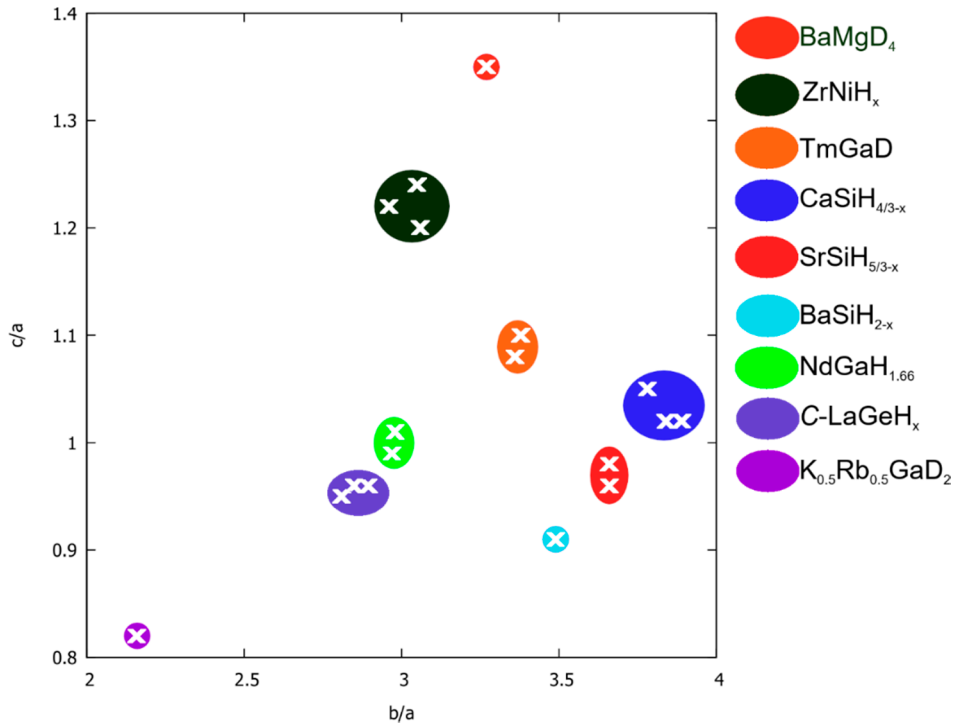

Figure 8. Structure map of different CrB type related hydrides regarding their lattice parameter ratios with different structure families indicated by colored areas; representatives listed in Table 4.

Table 4. Lattice parameter ratios of selected hydrides with crystal structures related to the CrB type.

Compound	Structure Type	*b*/*a*	*b*/*c*	*c*/*a*
ZrNiH [18]	ZrNiH	3.06	2.54	1.20
$ZrNiH_3$ [19]	$ZrNiH_3$	2.96	2.44	1.22
$TbNiD_{3.3}$ [16]	$TbNiD_{3.3}$	3.05	2.44	1.24
$BaMgD_4$ [47]	$ReBiO_4$	3.27	2.41	1.35
$K_{0.5}Rb_{0.5}GaD_2$ [22]	$K_{0.5}Rb_{0.5}GaD_2$	2.16	2.6	0.82
NdGeD [8]	*C*-LaGeD	2.81	2.93	0.95
$YSiH_x$	*C*-LaGeD	2.90	3.02	0.96
$ErSiH_x$	*C*-LaGeD	2.86	2.97	0.96
$TmSiH_x$	*C*-LaGeD	2.85	2.96	0.96
$LaGaD_{1.66}$	$NdGaD_{1.66}$	2.97	2.96	0.99
$NdGaD_{1.66}$ [20]	$NdGaD_{1.66}$	2.98	2.94	1.01
α-YGaH	α-TmGaD	3.36	3.09	1.08
α-TmGaD	α-TmGaD	3.38	3.06	1.10
$BaSiH_{2-x}$ [10]	$BaSiH_{2-x}$	3.49	3.79	0.91
$SrSiH_{5/3-x}$ [17]	$SrSiH_{5/3-x}$	3.66	3.80	0.96
$BaGeH_{5/3-x}$ [17]	$SrSiH_{5/3-x}$	3.66	3.74	0.98
$BaSnH_{4/3-x}$ [10]	$CaSiH_{4/3-x}$	3.78	3.58	1.05
$SrGeH_{4/3-x}$ [10]	$CaSiH_{4/3-x}$	3.84	3.75	1.02
$CaSiH_{4/3-x}$ [11]	$CaSiH_{4/3-x}$	3.89	3.81	1.02

A condensation of the polyanion (*a* contracted) is always accompanied by a distortion of the tetrahedra containing layer (*b* expanded) as seen for TmGaD and YGaD as well as for hydrides in the system *AeTt* (*Ae* = Ca, Sr, Ba; *Tt* = Si, Ge, Sn) [17]. A more detailed view is possible, when a second lattice parameter ratio is considered like *b*/*c* or *c*/*a*. Since *c* remains nearly unchanged, *c*/*a* correlates with condensation, while *b*/*c* describes the spatial demand of tetrahedra in *b* direction.

Hydrides of YSi and TmSi show lattice parameter ratios similar to NdGeD and can thus be assumed to crystallize in the *C*-LaGeD type structure as well (Table 4). Going from group 14 to 13

(*RETt*–*RE*Ga) the valence electron count decreases by one and for larger cations (La^{3+}, Nd^{3+}) one additional hydrogen atom is observed between the Ga chains, like in $LaGaH_{1.63(1)}$ and $NdGaH_{1.66}$, causing *b*/*a* and *c*/*a* ratio to increase. The expansion in *b* is due to the insertion of hydride ions in the Ln_3Ga_2 voids, while the shrinking of the *a* lattice parameter may indicate an interaction between the hydrogen and gallium atoms. A similar change in lattice parameter was observed for the hydrogenation of $LaGa_2$ and $CeGa_2$, where hydrogen atoms exhibit a similar coordination sphere [23,48]. Substituting one of the early lanthanides by a smaller atom—e.g., thulium or yttrium—results in stronger shrinking of the *a*, stronger expansion of the *b* lattice parameter and more pronounced puckering of H*Ln*$_4$ tetrahedral layers as compared to the corresponding tetrel containing compounds. This is indicated by the rising *b*/*a* value indicating the higher spatial demand along the crystallographic *b* direction. The puckering further results in a stronger contraction of the crystallographic *a* direction. Although $BaSiH_2$ has no distorted tetrahedral layer the *b*/*a* ratio is still higher than that of $TmGaD_{0.93(2)}$ and $YGaH_x$. One reason could be the size of Ba^{2+}, demanding a larger volume. The series of *AeTt*H_x. follows a similar trend with increasing condensation. An example with a very small *b*/*a* ratio is the Zintl phase $K_{0.5}Rb_{0.5}GaH_2$, which exhibits only covalently bonded hydrogen atoms in a polyethylene like polyanion and lacks hydrogen atoms inside polyhedra. These structural features result in a small *b*/*c* ratio. Even non Zintl phase CrB type hydrides (ZrNiH, $ZrNiH_3$, $TbNiH_3$, $BaMgD_4$), can be classified by this simple geometric scheme, showing different lattice parameter ratios due to different chemical bonding. This structure map enables categorization of different CrB type related hydrides and bears some predictive power for compounds where hydrogen positions have not been determined yet.

5. Summary

Six new rare earth containing Zintl phase hydrides were synthesized and characterized. For *RE*SiH_x (*RE* = Y, Er, Tm) the LaGeH structure type with filled tetrahedral RE_4 voids was assigned in analogy to known compounds with different *RE*. The crystal structures of $LaGaH_{1.63(1)}$ and $TmGaH_{0.93(2)}$ were solved from neutron diffraction on the deuterides. $LaGaH_{1.63(1)}$ crystallizes in the $NdGaH_{1.66}$ structure type and its structural and electronical features are comparable to $NdGaH_{1.66}$ and $GdGaH_x$. The Zintl phase hydrides *RE*GaH_x (*RE* = Y, Tm) exhibit a distorted filled CrB structure type with triple *a* lattice parameter. In these compounds only tetrahedral voids are filled with hydrogen atoms and a distortion of the pristine crystal structure occur. As a consequence, the distances between polyanionic gallium chains alternate, caused by the deformation of the tetrahedral layer. A structure map of CrB type related hydrides enables categorization according to lattice parameters ratios. This is a useful tool for crystal chemical discussions and for predictions when hydrogen positions have not been determined yet.

Supplementary Materials: The following are available online at http://www.mdpi.com/2073-4352/9/11/600/s1, Figure S1: Rietveld refinement of the crystal structure of $YSiH_x$, Figure S2: Rietveld refinement of the crystal structure of $ErSiH_x$, Figure S3: Rietveld refinement of the crystal structure of $TmSiH_x$, Figure S4: Thermal analyses (DSC) of TmGa at 1 MPa hydrogen pressure, Figure S5: Rietveld refinement of the crystal structure of α-$YGaH_x$, Figure S6: Crystal structures of LaGa, LaGaH and $LaGaH_{1.66}$ derived by DFT, Figure S7: Crystal structures of YGa and two YGaH modifications dervied by DFT, Table S1: Crystal structure of $YSiH_x$, Table S2: Crystal structure of $ErSiH_x$, Table S3: Crystal structure of $TmSiH_x$, Table S4: Crystal structure of $YGaH_x$, Table S5: k-point lattice for DFT calculations, Table S6: Structural parameters of LaGa derived by DFT, Table S7: Structural parameters of LaGaH derived by DFT, Table S8: Structural parameters of $LaGaH_{1.66}$ derived by DFT, Table S9: Structural parameters of YGa derived by DFT, Table S10: Structural parameters of YGaH (filled CrB type structure) derived by DFT, Table S11: Structural parameters of YGaH (distorted CrB type structure) derived by DFT.

Author Contributions: Conceptualization, H.K.; Methodology, H.K. and A.W.; Validation, A.W.; Formal Analysis, A.W.; Investigation, A.W. and T.C.H.; Resources, H.K.; Data Curation, A.W.; Writing—Original Draft Preparation, A.W. and H.K.; Writing—Review and Editing, H.K., A.W., and T.C.H.; Visualization, A.W.; Supervision, H.K.; Project Administration, H.K.; Funding Acquisition, H.K.

Funding: This work was founded by the Deutsche Forschungsgemeinschaft (Ko 1803/8).

Acknowledgments: We acknowledge support from the German Research Foundation (DFG) and Universität Leipzig within the program of Open Access Publishing. We are grateful to the Institute Laue-Langevin (Grenoble, France) for the allocation of neutron radiation beamtime.

Conflicts of Interest: The authors declare no conflict of interest.

References

1. Kohlmann, H. *Encyclopedia of Physical Science and Technology*, 3rd ed.; Meyers, R.A., Ed.; Academic Press: Cambridge, MA, USA, 2002; Volume 9, pp. 441–458.
2. Zintl, E.; Kaiser, H. Über die Fähigkeit der Elemente zur Bildung negativer Ionen. *Zeitschrift Anorganische Allgemeine Chemie* **1933**, *211*, 113–131. [CrossRef]
3. Schäfer, H.; Eisenmann, B.; Müller, W. Zintl-Phasen: Übergangsformen zwischen Metall- und Ionenbindung. *Angew. Chem.* **1973**, *85*, 742–760. [CrossRef]
4. Nesper, R. Chemische Bindungen—Intermetallische Verbindungen. *Angew. Chem.* **1991**, *103*, 805–834. [CrossRef]
5. Kurylyshyn, I.M.; Fässler, T.F.; Fischer, A.; Hauf, C.; Eickerling, G.; Presnitz, M.; Scherer, W. Probing the Zintl-Klemm Concept: A Combined Experimental and Theoretical Charge Density Study of the Zintl Phase CaSi. *Angew. Chem. Int. Ed.* **2014**, *53*, 3029–3032. [CrossRef] [PubMed]
6. Häussermann, U.; Kranak, V.F.; Puhakainen, K. Hydrogenous Zintl Phases: Interstitial Versus Polyanionic Hydrides. *Struct. Bond.* **2011**, *139*, 143–162. [CrossRef]
7. Chotard, J.-N.; Tang, W.S.; Raybaud, P.; Janot, R. Potassium Silanide ($KSiH_3$): A Reversible Hydrogen Storage Material. *Chem. Eur. J.* **2011**, *44*, 12302–12309. [CrossRef]
8. Werwein, A.; Auer, H.; Kuske, L.; Kohlmann, H. From Metallic *LnTt* (*Ln* = La, Nd; *Tt* = Si, Ge, Sn) to Electron-precise Zintl Phase Hydrides *LnTt*H. *Zeitschrift Anorganische Allgemeine Chemie* **2018**, *644*, 1532–1539. [CrossRef]
9. Huang, B.; Corbett, J.D. Intermetallic Hydrides as Zintl Phases: A_3TtH_2 Compounds (*A* = Ca, Yb; *Tt* = Sn, Pb) and Their Structural Relationship to the Corresponding Oxides. *Inorg. Chem.* **1997**, *36*, 3730–3734. [CrossRef]
10. Auer, H.; Guehne, R.; Bertmer, M.; Weber, S.; Wenderoth, P.; Hansen, T.C.; Haase, J.; Kohlmann, H. Hydrides of Alkaline Earth−Tetrel (AeTt) Zintl Phases: Covalent Tt−H Bonds from Silicon to Tin. *Inorg. Chem.* **2017**, *56*, 1061–1071. [CrossRef]
11. Wu, H.; Zhou, W.; Udovic, T.J.; Rush, J.J.; Yildirim, T. Structure and hydrogen bonding in $CaSiD_{1+x}$: Issues about covalent bonding. *Phys. Rev. B* **2006**, *74*, 224101. [CrossRef]
12. Björling, T.; Noréus, D.; Häussermannm, U. Polyanionic Hydrides from Polar Intermetallics AeE_2 (*Ae* = Ca, Sr, Ba; *E* = Al, Ga, In). *J. Am. Chem. Soc.* **2006**, *128*, 817–824. [CrossRef] [PubMed]
13. Björling, T.; Noréus, D.; Jansson, K.; Andersson, M.; Leonova, E.; Edén, M.; Hålenius, U.; Häussermann, U. SrAlSiH: A Polyanionic Semiconductor Hydride. *Angew. Chem. Int. Ed.* **2005**, *44*, 7269–7273. [CrossRef] [PubMed]
14. Dwight, A.E.; Downey, J.W.; Conner, R.A. Equiatomic compounds of Y and the lanthanide elements with Ga. *Acta Cryst.* **1967**, *23*, 860–862. [CrossRef]
15. Dürr, I.; Bauer, B.; Röhr, C. Lanthan-Triel/Tetrelide $La(Al,Ga)_x(Si,Ge)_{1-x}$. Experimentelle und theoretische Studien zur Stabilität intermetallischer 1:1-Phasen. *Zeitschrift Naturforschung B* **2011**, *66*, 1107–1115. [CrossRef]
16. Yaropolov, Y.L.; Andreenko, A.S.; Nikitin, S.A.; Agafonov, S.S.; Glazkov, V.P.; Verbetsky, V.N. Structure and magnetic properties of RNi (R=Gd, Tb, Dy, Sm) and $R_6M_{1.67}Si_3$ (R=Ce, Gd, Tb; M=Ni, Co) hydrides. *J. Alloys Compd.* **2011**, *509*, S830–S834. [CrossRef]
17. Auer, H.; Schlegel, R.; Oeckler, O.; Kohlmann, H. Structural and Electronic Flexibility in Hydrides of Zintl Phases with Tetrel-Hydrogen and Tetrel-Tetrel Bonds. *Angew. Chem. Int. Ed.* **2017**, *56*, 12344–12347. [CrossRef] [PubMed]
18. Westlake, D.G.; Shaked, H.; Mason, P.R.; Matsumoto, T.; Amano, M. Interstitial site occupation in ZrNiH. *J. Less-Common Met.* **1982**, *88*, 17–23. [CrossRef]
19. Korst, W.L. The crystal structure of $NiZrH_3$. *J. Phys. Chem.* **1962**, *66*, 370–372. [CrossRef]
20. Ångstrom, J.; Johansson, R.; Sarkar, T.; Sørby, M.H.; Zlotea, C.; Andersson, M.S.; Nordblad, P.; Scheicher, R.H.; Häussermann, U.; Sahlberg, M. Hydrogenation-Induced Structure and Property Changes in the Rare-Earth Metal Gallide NdGa: Evolution of a $[GaH]^{2-}$ Polyanion Containing Peierls-like Ga−H Chains. *Inorg. Chem.* **2016**, *55*, 345–352. [CrossRef]

21. Nedumkandathil, R.; Kranak, V.F.; Johansson, R.; Ångström, J.; Balmes, O.; Andersson, M.S.; Nordblad, P.; Scheicher, R.H.; Sahlberg, M.; Häussermann, U. Hydrogenation induced structure and property changes in GdGa. *J. Solid State Chem.* **2016**, *239*, 184–191. [CrossRef]
22. Fahlquist, H.; Noréus, D.; Sørby, M.H. Varying the Alkali-Metal Radii in $(K_xRb_{1-x})_n[GaH_2]_n$ $(0 \leq x \leq 1)$ Reorients a Stable Polyethylene-Structured $[GaH_2]_n^{n-}$ Anionic Chain. *Inorg. Chem.* **2013**, *52*, 4771–4773. [CrossRef] [PubMed]
23. Werwein, A.; Benndorf, C.; Bertmer, M.; Franz, A.; Oeckler, O.; Kohlmann, H. Hydrogenation Properties of $LnAl_2$ (*Ln* = La, Eu, Yb), $LaGa_2$, $LaSi_2$ and the Crystal Structure of $LaGa_2H_{0.71(2)}$. *Crystals* **2019**, *9*, 193. [CrossRef]
24. Hansen, T.C.; Henry, P.F.; Fischer, H.E.; Torregrossa, J.; Convert, P. The D20 instrument at the ILL: A versatile high-intensity two-axis neutron diffractometer. *Meas. Sci. Technol.* **2008**, *19*, 34001. [CrossRef]
25. Götze, A.; Auer, H.; Finger, R.; Hansen, T.C.; Kohlmann, H. A sapphire single-crystal cell for in situ neutron powder diffraction of solid-gas reactions. *Physica B (Amst. Neth.)* **2018**, *551*, 395–400. [CrossRef]
26. Kohlmann, H.; Finger, R.; Goetze, A.; Hansen, T.; Pflug, C.; Werwein, A. *Hydrides of the Zintl Phase TmGa*; Institut Laue-Langevin (ILL): Grenoble, France, 2018. [CrossRef]
27. Rietveld, H.M. Line profiles of neutron powder-diffraction peaks for structure refinement. *Acta Cryst.* **1967**, *22*, 151–152. [CrossRef]
28. Rietveld, H.M. A profile refinement method for nuclear and magnetic structures. *J. Appl. Crystallogr.* **1969**, *2*, 65–71. [CrossRef]
29. Bruker AXS, TOPAS© Version 5. Available online: https://www.bruker-axs.com (accessed on 30 October 2018).
30. Rodrıguez-Carvajal, J. Recent advances in magnetic structure determination by neutron powder diffraction. *Physica B (Amst. Neth.)* **1993**, *192*, 55–69. [CrossRef]
31. Rodrıguez-Carvajal, J. *FullProf.2k, Version 5.30—Mar2012-ILL JRC*; Institut Laue-Langevin: Grenoble, France, 2018.
32. *VESTA—Visualisation for Electronic and Structural Analysis, Version 3.3.1*; Koichi Momma and Fujio Izumi: Ibaraki, Japan, 2018.
33. Momma, K.; Izumi, F. VESTA 3 for three-dimensional visualization of crystal, volumetric and morphology data. *J. Appl. Crystallogr.* **2011**, *44*, 1272–1276. [CrossRef]
34. Abinit v. 8.8.2, GNU General Public License. Available online: http://www.abinit.org (accessed on 14 June 2018).
35. Gonze, X.; Beuken, J.-M.; Caracas, R.; Detraux, F.; Fuchs, M.; Rignanese, G.-M.; Sindic, L.; Verstraete, M.; Zerah, G.; Jollet, F.; et al. First-principles computation of material properties: The ABINIT software project. *Comput. Mater. Sci.* **2002**, *25*, 478–492. [CrossRef]
36. Gonze, X. A brief introduction to the ABINIT software package. *Zeitschrift Kristallographie Cryst. Mater.* **2005**, *220*, 558–562. [CrossRef]
37. Gonze, X.; Amadon, B.; Anglade, P.-M.; Beuken, J.-M.; Bottin, F.; Boulanger, P.; Bruneval, F.; Caliste, D.; Caracas, R.; Côté, M.; et al. ABINIT: First-principles approach to material and nanosystem properties. *Comput. Phys. Commun.* **2009**, *180*, 2582–2615. [CrossRef]
38. Gonze, X.; Jollet, F.; Araujo, F.A.; Adams, D.; Amadon, B.; Applencourt, T.; Audouze, C.; Beuken, J.-M.; Bieder, J.; Bokhanchuk, A.; et al. Recent developments in the ABINIT software package. *Comput. Phys. Commun.* **2016**, *205*, 106–131. [CrossRef]
39. Perdew, J.P.; Burke, K.; Ernzerhof, M. Generalized Gradient Approximation Made Simple. *Phys. Rev. Lett.* **1996**, *77*, 3865–3868. [CrossRef] [PubMed]
40. Blöchl, P.E. Projector augmented-wave method. *Phys. Rev. B* **1994**, *50*, 17953–17979. [CrossRef] [PubMed]
41. JTH PAW Atomic Datasets, Version 1.0. Available online: https://www.abinit.org/downloads/PAW2 (accessed on 28 March 2019).
42. Jollet, F.; Torrent, M.; Holzwarth, N. Generation of Projector Augmented-Wave atomic data: A 71 element validated table in the XML format. *Comput. Phys. Commun.* **2014**, *185*, 1246–1254. [CrossRef]
43. Monkhorst, H.J.; Pack, J.D. Special points for Brillouin-zone integrations. *Phys. Rev. B* **1976**, *13*, 5188–5192. [CrossRef]
44. Fischer, P.; Haelg, W.; Schlapbach, L.; Yvon, K. Neutron and X-ray diffraction investigation of deuterium storage in La_7Ni_3. *J. Less-Common Met.* **1978**, *60*, 1–9. [CrossRef]

45. Udovic, T.J.; Huang, Q.; Santoro, A.; Rush, J.J. The nature of deuterium arrangements in YD_3 and other rare-earth trideuterides. *Zeitschrift Kristallographie Cryst. Mater.* **2008**, *223*, 687–704. [CrossRef]
46. Gschneidner, K.A., Jr.; Eyring, L. (Eds.) *Handbook on the Physics and Chemistry of Rare Earths*; North-Holland Publishing: Amsterdam, The Netherlands, 1978.
47. Gingl, F.; Yvon, K.; Vogt, T. Synthesis and crystal structure of $BaMgH_4$: A centrosymmetric variant of $SrMgH_4$. *J. Alloys Compd.* **1997**, *256*, 155–158. [CrossRef]
48. Shashikalaa, K.; Sathyamoorthy, A.; Raj, P.; Dhar, S.K.; Malik, S.K. Structure and magnetic properties of $CeGa_2D_{0.6}$ system. *J. Alloys Compd.* **2007**, *436*, 19–22. [CrossRef]